RSC Advances

PAPER

View Article Online
View Journal | View Issue

Cite this: *RSC Adv.*, 2019, **9**, 31035

Comparative study of mesoporous $Ni_xMn_{6-x}Ce_4$ composite oxides for NO catalytic oxidation

Li Weiman,[abcd] Liu Haidi,[a] Zhang Min[ab] and Chen Yunfa*[ad]

In this work, a series of mesoporous $Ni_xMn_{6-x}Ce$ ternary oxides were prepared to investigate their NO catalytic oxidation ability. The sample $Ni_2Mn_4Ce_4$ showed a 95% NO conversion at 210 °C (GHSV, ~80 000 h^{-1}). Characterization results showed the good catalytic performance of $Ni_2Mn_4Ce_4$ was due to its high specific surface area, more surface oxygen and high valance manganese species, which can be ascribed to the incorporation of three elements. Based on the results of XRD, H_2-TPR, O_2-TPD and XPS, we confirmed the existence of $Ni^{3+} + Mn^{3+} \rightarrow Ni^{2+} + Mn^{4+}$, $Ce^{4+} + Ni^{2+} \rightarrow Ce^{3+} + Ni^{3+}$ in $Ni_2Mn_4Ce_4$, and the oxidation–reduction cycles were proved to be helpful for NO oxidation. The results from an *in situ* DRIFTS study indicated the presence of bidentate nitrate and monodentate nitrate species on the catalyst's surface. The nitrate species were proved to be intermediates for NO oxidation to NO_2. A nitrogen circle mechanism was proposed to explain the possible route for NO oxidation. Nickel introduction was also helpful to improve the SO_2 resistance of the NO oxidation reaction. The activity drop of $Ni_2Mn_4Ce_4$ was 13.15% in the presence of SO_2, better than Mn_6Ce_4 (25.29%).

Received 5th July 2019
Accepted 23rd September 2019

DOI: 10.1039/c9ra05098a

rsc.li/rsc-advances

1 Introduction

Nitrogen monoxide, nitrogen dioxide and nitrous oxide, known as nitrogen oxides (NO_x) are important pollutants in causing a series of environmental problems, such as acid rain, photochemical smog, and ozone depletion.[1] Many technologies have been developed to deal with NO_x, such as NH_3-selective catalytic reduction, ozone assisted NO oxidation, and NO_x storage reduction.[2] The oxidation of NO to NO_2 is an important step for almost all the NO abatement technologies; for example, NO oxidation can enhance NH_3-SCR to follow a fast SCR mechanism,[3] and in the wet scrubbing method, the conversion of NO to NO_2 is helpful to increase NO_x removal efficiency.[4,5] Therefore, much effort has been made to develop catalysts with good NO oxidation ability.

Several types of catalysts, including noble metal catalysts,[6] supported catalysts,[7] and multi-metal oxide catalysts[8,9] were reported to have good catalytic activities under different reaction conditions. Multi-metal composites have good catalytic activities in the low and middle temperature range (100–320 °C), which are suitable to be applied in flue gas. Among them, manganese and ceria composite oxides have been reported several times for their excellent redox properties, oxygen storage capacity, and excellent performance in NO oxidation.[10] However, the NO oxidation ability of Mn–Ce composites is severely affected by SO_2 in real application condition. Researches confirmed that SO_2 can react with manganese species to form sulfate salts, leading to irreversible activity decrease.[11] It is commonly accepted that in the process of NO catalytic oxidation, NO were firstly adsorbed on the surface of catalysts to form nitrates; and then nitrates were reacted with O_2 to form NO_2.[9,12] On one hand, the introduction of SO_2 in the flue gas may influence the formation of different types of nitrates. On the other hand, the type of nitrates formed on the catalysts surface are related to surface oxygen species and manganese valence, which were influenced by morphology, element dopant *et al.* To get catalysts with excellent catalytic performance and good SO_2 resistance, a second/third element dopant is a facile way. Several studies have reported a third dopant to Mn–Ce composites to improve their NO oxidation performance, because the regulated manganese and oxygen species.[11b,13] However, few were focused on both catalytic performance and SO_2 tolerance. The goal of this study is to improve both NO oxidation ability and SO_2 tolerance of classical Mn–Ce composites. Nickel was selected as the third dopant, because introduction of nickel lead to more surface oxygen and regulate metal valence. Moreover, SO_2-TPD confirmed that introduction of nickel to Mn–Ce composites was helpful to reduce SO_2 adsorption.[14] In this study, we fabricated a series of $Ni_xMn_{6-x}Ce_4$ ternary oxides to further discuss interaction among three elements. The $Ni_2Mn_4Ce_4$ catalysts showed best low temperature activity and good SO_2 resistance.

[a]State Key Laboratory of Multi-phase Complex Systems, Institute of Process Engineering, Chinese Academy of Sciences, Beijing 100190, China. E-mail: chenyf@ipe.ac.cn

[b]University of Chinese Academy of Sciences, No. 19A Yuquan Road, Beijing 100049, China

[c]Zhongke Langfang Institute of Process Engineering, Langfang Economic & Technical Development Zone, Fenghua Road No 1, Hebei, China

[d]CAS Center for Excellence in Urban Atmospheric Environment, Xiamen 361021, China

2 Experimental sections

2.1 Catalysts preparation

Previous studies[15,16] had shown that Mn/Ce composites with a molar ratio equal or slightly more than 1 showed a most active catalytic activity; similar with our previous work, in which the catalyst with a molar ratio of Mn/Ce = 6/4 had the best catalytic performance, because strong interaction between manganese and ceria. As a result, nickel substituted Mn_6Ce_4 catalysts were prepared, denoted as $Ni_xMn_{6-x}Ce_4$, where x represented the relative molar ratio of Ni and Mn. All chemicals used in this study, such as $Mn(NO_3)_2$ (50 wt%), $Ce(NO_3)_3 \cdot 6H_2O$, $Ni(NO_3)_2 \cdot 6H_2O$ and NaOH were purchased from Xilong Cop. (China) and used without further purification. The mesoporous composites were prepared through a nano-casting method by employing KIT-6 as templates. KIT-6 silica was prepared as previously reported studies.[17] In a typical procedure, 1.0 g KIT-6 was suspended in 80 mL *n*-hexane and stirred at room temperature for 2 h. Then a mixed solution of $Mn(NO_3)_2$, $Ni(NO_3)_2$ and $Ce(NO_3)_3$ was added slowly with vigorous stirring. After stirred overnight, the mixture was filtered and dried at 80 °C for 24 h. The obtained powder was calcined at 550 °C for 4 h, with a heating rate of 2 °C min^{-1} in air. Finally, the sample was treated three times with a 2 M NaOH solution, washed to pH ~ 7 and dried at 80 °C.

2.2 Catalytic activity evaluation

The NO catalytic oxidation activity tests of prepared samples were performed in a fix-bed quartz tubular reactor. 100 mg catalysts (40–60 mesh) were placed in the reactor, with a weight hourly space velocity (WHSV) of 60 000 mL g^{-1} h^{-1} (GHSV ~ 85 000 h^{-1}). The feed gas consisted of 200 ppm NO, 5% O_2, 200 ppm SO_2 (when used) and balance N_2, with a flow rate of 0.1 L min^{-1}. The concentration of NO and NO_2 were monitored by a two channel CLD60 (Eco physics) instrument. NO conversion rate was calculated by:

$$\text{NO conversion} = (NO_{in} - NO_{out})/NO_{in} \times 100\%$$

2.3 Characterization

XRD patterns were recorded on a PANalytical X'Per PRO X-ray diffraction in 2θ from 5° to 90° with a scanning step of 0.0334°. The specific surface area and pore size distributions of all catalysts were obtained according to the Brunauer–Emmett–Teller (BET) and Barrett–Joyner–Halenda (BJH) methods, respectively, using N_2 adsorption–desorption method on an automatic surface analyzer (SSA-7300, BJ-Builder, China) at 77 K. Each sample was pre-degassed at 150 °C for 3 h. H_2 temperature-programmed reduction (H_2-TPR) was conducted on a Micromeritics Chemisorb 2720 analyzer (Micromeritics, USA) at a heating rate of 10 °C min^{-1} with 5% H_2/Ar gas. The H_2 consumption was recorded continuously to investigate reduction abilities. O_2-TPD was performed on a BJ-Builder 1200 apparatus; 100 mg 40–60 mesh sample was firstly heated to 500 °C and kept for 30 min in He flow to remove surface adsorptive species. After cooling down to 50 °C, the sample was treated in O_2 for 1 h, and then blew with He for 30 min. Finally, the TCD signal was collected to 900 °C at 10 °C min^{-1} in 30 mL min^{-1} He flow. Surface species of as-prepared catalysts were determined by X-ray photoelectron spectroscopy (XPS) using a XLESCALAB 250 Xi electron spectrometer (Thermo Scientific, USA) with monochromatic Al Kα radiation (1486.6 eV). A Bruker Vertex 70 spectrometer (Bruker, USA) equipped with diffuse reflectance accessory (PIKE, and MCT/A detector cooled by liquid nitrogen) was used for recording the *in situ* DRIFT spectra of the samples. The sample was pretreated at 300 °C for 2 h in N_2 (50 mL min^{-1}). The reaction system was cooled to 200 °C in N_2, and the spectra were collected as background. The feed gas was 250 ppm NO, 5% O_2 (when used), and balance N_2, with a flow rate of 0.1 L min^{-1}. When the spectra was pre-adsorbed by NO or NO + O_2, then purged by N_2 for 30 min to remove weakly adsorbed species, and finally recorded by accumulating 32 scans at a resolution of 4 cm^{-1}.

3 Results and discussions

3.1 Catalytic performances

The NO–NO_2 catalytic activities of as-prepared catalysts were tested and compared from 120 °C to 360 °C, and the results were shown in Fig. 1. NO conversion rate over all catalysts firstly raised to a peak with the temperature increasing; then NO conversion rate decreased as the reaction temperature continuous increasing. $Ni_1Mn_5Ce_4$ and $Ni_2Mn_4Ce_4$ reached its highest NO conversion of 90% and 95% at 210 °C, respectively. Mn_6Ce_4 and $Ni_3Mn_4Ce_4$ reached their maximum NO conversion of 85% and 81% at 240 °C, respectively. $Ni_4Mn_2Ce_4$ and $Ni_1Mn_5Ce_4$ had a similar NO conversion of 77% at 270 °C. Ni_6Ce_4 performed the worst NO conversion, with its maximum conversion of 60% at 300 °C. The catalytic activity of different samples varied at low temperature, and mainly followed the sequence of $Ni_2Mn_4Ce_4$ > $Ni_1Mn_5Ce_4$ > Mn_6Ce_4 > $Ni_3Mn_3Ce_4$ > $Ni_4Mn_2Ce_4$ > $Ni_5Mn_1Ce_4$ > Ni_6Ce_4. The sample $Ni_2Mn_4Ce_4$ can reach its maximum NO conversion of 95% at 210 °C, better than previous studies shown in Table 1.

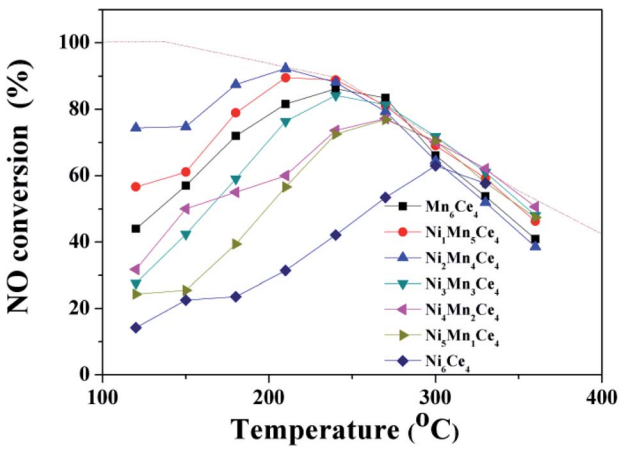

Fig. 1 NO catalytic oxidation performance of $Ni_xMn_{6-x}Ce_4$ composites.

Table 1 Summary of the properties of catalysts in literature

Catalyst	Preparation method	Reaction conditions	NO conversion	References
γ-MnO_2	Hydro-thermal synthesis, powder	500 ppm NO, 5% O_2, 24 000 h^{-1}	250 °C, 86.4%	19
MnO_2	Precipitation method, powder	500 ppm NO, 5% O_2, 48 000 mL g^{-1} h^{-1}	210 °C, 91%	12*a*
Ce–Co composite oxides	Sol–gel method, powder	300 ppm NO, 10% O_2, 20 000 h^{-1}	230 °C, 93%	18
Urchin-like γ-MnO_2	Hydro-thermal synthesis, powder	500 ppm NO, 10% O_2, 75 000 h^{-1}	280 °C, 88%	20
$Ni_2Mn_4Ce_4$	Nano-casting method, powder	200 ppm NO, 5% O_2, 60 000 mL g^{-1} h^{-1}	210 °C, 95%	This work

As the conversion of NO to NO_2 is an exothermal reaction, and the reaction is thermodynamic limited at higher temperature.[12,18] The thermodynamic equilibrium of NO to NO_2 under the same condition was shown in dashed line. At high temperature, the catalytic activity was closely related to the equilibrium, which indicated the reaction was thermodynamic control. However, it can be seen that the low temperature catalytic activity was related to the relative ratios of manganese and nickel. To investigate the effect, further characterizations were applied and discussed in the following parts.

3.2 Physicochemical properties

3.2.1 Structural characterization. The structural properties of all oxides were examined by XRD, and the results were shown in Fig. 2. All the catalysts exhibited peaks associated with CeO_2 (JCPDS 00-001-0800). The peaks located at 28.6°, 33.2°, 47.8°, 59.6°, corresponding to the (111), (200), (220), and (222) planes of CeO_2, respectively. No peaks related to MnO_x were observed, indicating in all samples manganese incorporated into ceria lattice, similar with previous study.[21] When $x > 4$, the peaks ($Ni_5Mn_1Ce_4$ and Ni_6Ce_4) located at 37.4°, 43.4°, 62.7°, 75.6°, 78.6°, can be assigned to (111), (200), (220), (311), (222) planes of NiO (JCPDS 00-001-1239). At a high Ni level, separate phase NiO were formed in the composites. But when $x \leq 4$, there were no peaks of NiO. At a low Ni level, as there is no NiO related peaks, nickel may exist in two forms: (i) NiO clusters in ceria lattice, and (ii) Ni^{2+} in ceria lattice. C. Lamonier[22] reported in Ni–Ce composites, when Ni/Ce ≤ 0.5, Ni^{2+} can entrance ceria lattice to substitute Ce^{4+}, which can be proved by XRD peak shift of ceria. As there were peak shifts in all samples shown in Fig. 2(B), manganese and part of nickel may both can enter ceria lattice. The ceria lattice constants obtained from XRD reflections of all samples were shown in Fig. 2(C), and it may be influenced both by manganese and nickel in this study. With x increased from 0 to 6, the calculated lattice constants gradually increased, and then was stable at ~0.5411 nm, which was close

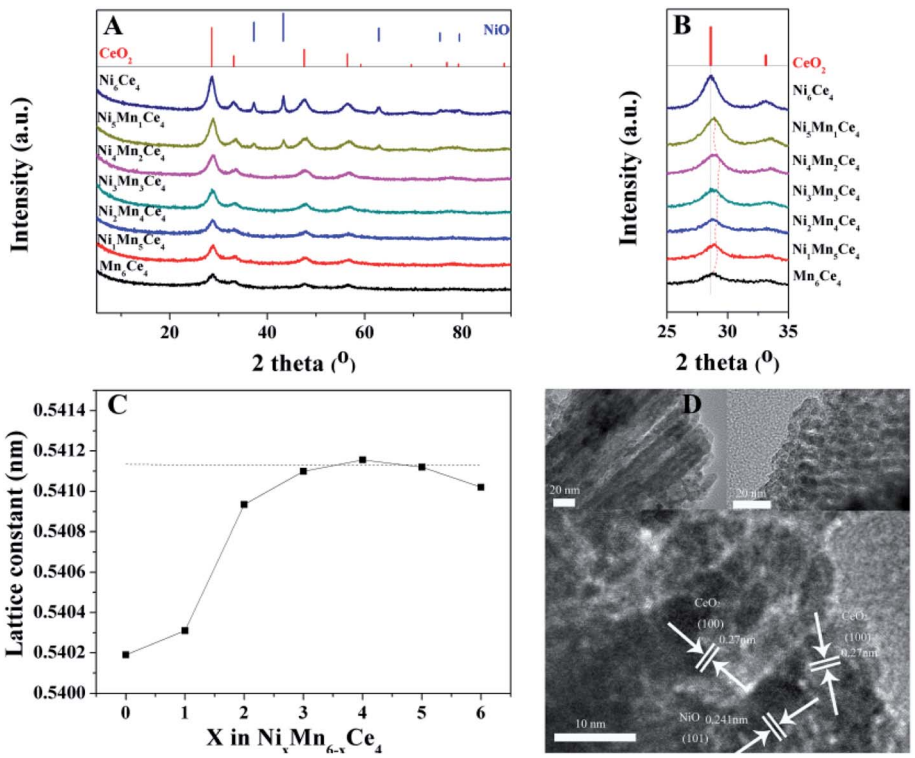

Fig. 2 (A) X-ray diffraction patterns of $Ni_xMn_{6-x}Ce_4$ composites; (B) magnification of a peak assigned to CeO_2 (111); (C) CeO_2 lattice constants of different samples as a function of x; and (D) TEM and HRTEM images of $Ni_2Mn_4Ce_4$.

to the lattice constant of pure CeO_2. For $Ni_5Mn_1Ce_4$ and Ni_6Ce_4, which had obvious NiO peaks, the NiO lattice constants were 0.2953 nm and 0.2955 nm, respectively, similar with pure NiO (0.2955 nm). This suggested that at a high nickel level, nickel and ceria were formed separate phases, similar with Zhu's report.[23] For $Ni_2Mn_4Ce_4$, TEM images (Fig. 2(D)) showed that ~10 nm NiO particles dispersed in CeO_2 matrix, and no evidence of MnO_x were observed. Combined with conclusion form peak shift study, at a low nickel content, nickel oxide was present in ceria, probably in the form of nano-clusters, and with an amount of Ni^{2+}, as a result, there was no peak related to NiO. Based on above analysis, the lattice constants variation when $x < 3$ may probably due to manganese and nickel ions, which can enter ceria lattice to form solid solution, because the ionic radius of Mn^{4+} and Ni^{2+} are smaller than Ce^{4+}. For $Ni_2Mn_4Ce_4$, manganese and part of nickel ions may enter ceria lattice to form solid solution, while NiO cluster may well dispersed in the matrix of solid solution.

As surface area and pore size of catalysts contributed much to catalytic activity, the N_2 adsorption–desorption isotherms and pore size distributions were shown in Fig. 3; the specific area and average pore size were also summarized in Table 2. All the catalysts showed a type IV isotherm with a H_3 hysteresis loop, indicating the existence of mesoporous structure. The specific surface area followed a sequence of $Ni_2Mn_4Ce_4$ > $Ni_1Mn_5Ce_4$ > $Ni_3Mn_3Ce_4$ > $Ni_4Mn_2Ce_4$ > Mn_6Ce_4 > $Ni_4Mn_2Ce_4$ > $Ni_5Mn_1Ce_4$ > Ni_6Ce_4. It can be seen that the surface area of the catalysts firstly increased with nickel addition, and then decreased, indicating the three elements incorporated with each other. The $Ni_2Mn_4Ce_4$ catalyst had the largest surface area, which may also have more active sites for NO adsorption and oxidation, consistent with NO catalytic activity. It was interesting that when $x < 4$, nickel content increase could enlarge surface area; when $x > 4$, surface area decreased with further nickel addition. The results were consistent with XRD patterns, because when $x > 4$, the high crystallinity was a reason for surface area decrease. As the samples all presented only CeO_2 phase when $x < 4$, it was more meaningful to discuss these samples. The specific area of samples from $Ni_1Mn_5Ce_4$ to $Ni_4Mn_2Ce_4$ were larger than Mn_6Ce_4, so it is reasonable to attribute the change to the introduction of nickel into Mn–Ce system. The H_2-TPR and XPS results in the following parts would also support our hypothesis.

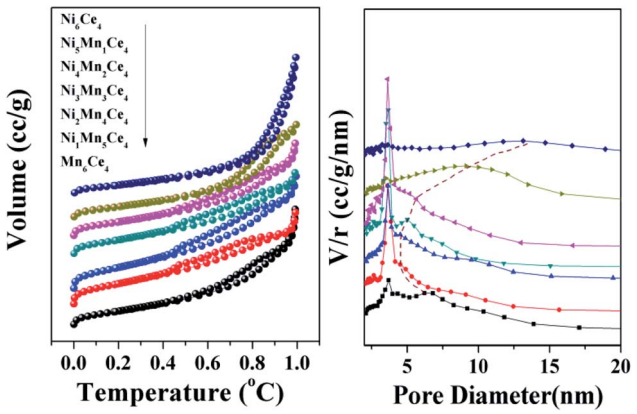

Fig. 3 N_2 adsorption–desorption isotherm and pore size distributions of composites, and their specific surface area data.

3.2.2 Temperature programmed reduction/desorption. The H_2-TPR was used to investigate redox properties of the catalysts, which were usually related to catalytic activities. As shown in Fig. 4(A), the Mn_6Ce_4 sample presented three main peaks, centered at 297 °C, 405 °C and 485 °C, which can be assigned to the reduction of $Mn^{4+} \rightarrow Mn^{3+}$, $Mn^{3+} \rightarrow Mn^{2+}$ and $Ce^{4+} \rightarrow Ce^{3+}$, respectively.[24] When x increased to 2, the peak related to $Mn^{4+} \rightarrow Mn^{3+}$ shifted to lower temperature range (262 °C and 234 °C), indicating the improvement of reduction properties; this may be caused by increase of high valance manganese species.[25] There was a new peak appeared at ~358 °C for $Ni_2Mn_4Ce_4$, and with increasing x, the peak intensity becomes stronger. We certainly ascribed the peak to the reduction of NiO_x.[26] When x was larger than 3, a new shoulder peak at ~300 °C appeared; however, the peak disappeared when manganese was fully substituted by nickel. This small shoulder peak may be related to the reduction of manganese species, indicating the further increase of manganese valence caused by nickel addition. There was a board peak at 365 °C for Ni_6Ce_6, which can be ascribed to the overlap of reduction of nickel species and ceria species. From the lower reduction temperature of different samples, it was interpreted that the corporation of Mn, Ce, Ni reached a maximum for $Ni_2Mn_4Ce_4$, therefore greatly enhanced the reducibility of catalysts.

The O_2-TPD spectra were shown in Fig. 4(B), and were used to determine the oxygen species in different samples. The O_2-desorption spectra were divided into three segments, according to their desorption temperature.[27] The peaks < 400 °C (denoted

Table 2 Summarized physical properties and surface species ratios of all samples

Samples	BET[a] ($m^2\ g^{-1}$)	Pore volume[b] ($mL\ g^{-1}$)	Pore diameter[a] (nm)	O_{ads}[c]/(O_{latt} + O_{ads})	Ni^{3+}/Ni^{2+c}	Mn^{3+}/Mn^{4+c}	Ce^{3+}/Ce^{4+c}
Mn_6Ce_4	152.116	0.3955	10.70	0.81	—	0.68	0.27
$Ni_1Mn_5Ce_4$	208.031	0.3051	7.28	0.91	11.15	0.64	0.34
$Ni_2Mn_4Ce_4$	221.013	0.3867	6.24	0.98	3.46	0.42	0.28
$Ni_3Mn_3Ce_4$	160.861	0.2849	8.66	0.88	3.74	0.51	0.56
$Ni_4Mn_2Ce_4$	159.982	0.3237	7.22	0.94	1.87	0.50	0.33
$Ni_5Mn_1Ce_4$	122.246	0.3285	11.20	0.90	0.57	0.81	0.45
Ni_6Ce_4	108.082	0.5125	17.64	0.91	0.35	—	0.41

[a] Calculated by BET method, obtained from N_2 adsorption at 77 K. [b] Determined by adsorption capacity at relative pressure of $P/P_0 = 0.99$. [c] Calculated from XPS data.

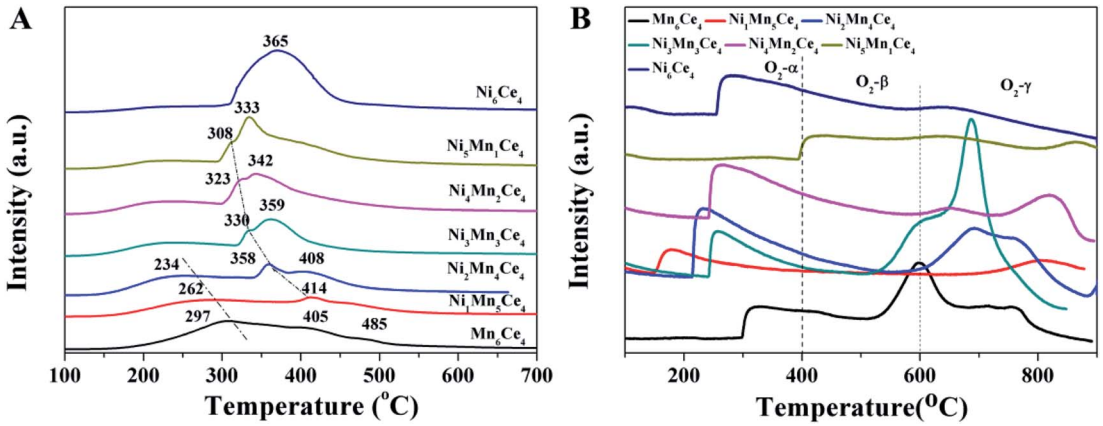

Fig. 4 (A) The H_2-TPR and (B) O_2-TPD profile of different catalysts.

as O_2-α) was ascribed to the desorption of weakly adsorbed oxygen species. The peaks between 400 and 600 °C (O_2-β) were related to surface non-stoichiometric oxygen desorption.[28] And the peaks > 600 °C (O_2-γ) represented that the remained lattice oxygen was continuously declined, indicating higher valence of metal ions were reduced to lower valence. As the reaction temperature of NO oxidation in this study was lower than 400 °C, it was more meaningful to discuss O_2-α. The peak areas related to O_2-α for samples $Ni_xMn_{6-x}Ce_4$ (x from 0 to 6) were 6381, 7235, 8793, 6125, 5006, 236, and 6104, respectively. $Ni_2Mn_4Ce_4$ exhibited the most O_2-α species, and the result was consistent with XPS data in the next part.

3.2.3 Surface species valance analysis. In order to investigate details of surface species and obtain more information about cooperation among three elements, XPS spectra of different samples have been recorded and fitted, as shown in Fig. 5. The O 1s spectra can be fitted into three peaks as shown in Fig. 5(A). The peak centered at 529.7 eV was assigned to surface lattice oxygen (O_α), and the peaks at 531.4 eV and 533.1 eV can be assigned to surface adsorbed oxygen (O_β) and surface weakly adsorbed water (O_γ), respectively.[29] Because of mesoporous structure, the intensity of O_γ peak of all catalysts was much stronger than O_α and O_β, indicating much weakly adsorbed water on surface. The ratios of $O_\beta/(O_\alpha + O_\beta)$ were shown in Table 2. It is accepted that surface oxygen species are important in catalytic oxidation process.[30] The $Ni_2Mn_4Ce_4$ catalyst exhibited the largest $O_\beta/(O_\alpha + O_\beta)$ ratio, leading to the maximum NO oxidation activity.

Fig. 5(B) showed the Mn 2p spectra of $Ni_xMn_{6-x}Ce_4$ ($x = 0$–6), and Mn $2p_{3/2}$ can be de-convoluted into two peaks. The peaks at 643.2 eV and 641.4 eV can be assigned to Mn^{4+} and Mn^{3+}, indicating a mixed valence manganese state.[31] As shown in Table 2, the ratio of Mn^{3+}/Mn^{4+} was associated with Ni/Mn molar ratio. $Ni_2Mn_4Ce_4$ showed the smallest proportion of Mn^{3+}/Mn^{4+}, indicating more high valance Mn species in it. Furthermore, the catalytic performance sequence is consistent with Mn^{3+}/Mn^{4+}, indicating high valance manganese may be the active sites for NO oxidation.

The Ni 2p XPS spectra was convoluted into three peaks in Fig. 5(C). The peaks can be assigned to the main peak of Ni 2p

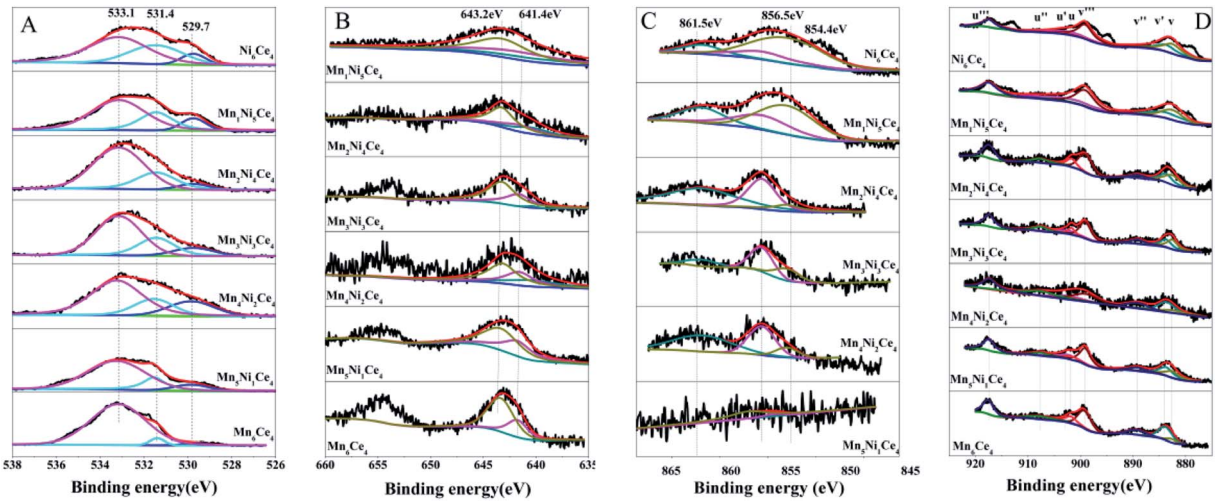

Fig. 5 The XPS spectra of $Ni_xMn_{6-x}Ce$ catalysts, (A) O 1s, (B) Mn 2p, (C) Ni 2p and (D) Ce 3d.

and two satellite peaks, which were located at 854.4 eV, 856.5 eV and 861.5 eV, respectively. The peak at 854.4 eV (with satellite 861.5 eV) was corresponding to Ni^{2+} species;[32] and the peak at 856.5 eV origins from Ni^{3+} species.[33] The Ni^{3+}/Ni^{2+} ratios of different samples were summarized in Table 1. When x was less than 3, the Ni^{3+}/Ni^{2+} firstly decreased and then increased. $Ni_2Mn_4Ce_4$ had the lowest Ni^{3+}/Ni^{2+} and Mn^{3+}/Mn^{4+}, indicating the existence of $Ni^{3+} + Mn^{3+} \rightarrow Ni^{2+} + Mn^{4+}$. However, when x was more than 3, Ni^{3+}/Ni^{2+} decreased sharply, indicating nickel species were mainly existed in the form of Ni^{2+}. This was consistent with XRD results, with the appearance of NiO peaks. The results showed that the addition of nickel could regulate the manganese valence, especially when $x < 3$. When $x > 3$, nickel oxide was hard to form solid solution with ceria, therefore leading to separate phase of NiO and CeO_2.

The Ce 3d spectra can be decomposed into eight peaks, as shown in the assignments of Fig. 5(D). According to literatures, The two bands labeled as v′ and u′ corresponded to Ce^{3+}, and the other six bands can be assigned to Ce^{4+}.[34] The Ce^{3+}/Ce^{4+} ratios were summarized in Table 1. Surprisingly, although molar ratio of cerium didn't change, the Ce^{3+}/Ce^{4+} ratios varied among different samples. This indicated there was also an interaction between cerium, nickel and manganese. Compared with other samples, $Ni_2Mn_4Ce_4$ presented lowest Ce^{3+}/Ce^{4+} ratio. More surface Ce^{4+} species would facilitate $Ni^{2+} + Ce^{4+} \rightarrow Ce^{3+} + Ni^{3+}$, therefore enhancing the reaction of $Ni^{3+} + Mn^{3+} \rightarrow Ni^{2+} + Mn^{4+}$.

From the above characterizations, it can be concluded $Ni_2Mn_4Ce_4$ exhibited biggest specific surface area, high ratio of Mn^{4+}, which can make it more productive in NO catalytic oxidation.

3.3 *In situ* DRIFTs study

As $Ni_2Mn_4Ce_4$ presented the best NO catalytic oxidation activity, a series of *in situ* DRIFTs experiments were investigated in order to study NO and/or O_2 adsorption behaviors.

3.3.1 NO adsorption behaviors on $Ni_2Mn_4Ce_4$. Fig. 6(A) exhibited the *in situ* DRIFTs spectra of $Ni_2Mn_4Ce_4$ catalysts exposed to NO + O_2/N_2 for 30 min at different temperatures, several bands at 1651, 1635, 1625, 1577, 1556, 1541, 1519, 1505, 1487 and 1309 cm^{-1} were detected. The bands at 1651, 1635, and 1625 cm^{-1} can be assigned to adsorbed NO_2.[20,35] The bands at 1577, 1556, 1541, 1505, 1487 cm^{-1} were ascribed to bidentate nitrate;[36] and the bands at 1519 and 1309 cm^{-1} can be assigned to monodentate nitrate.[20] Different from previous reports, the intensity of bands related to adsorbed NO_2 were much high, which may be due to the large surface area of the catalyst. The NO_2 were adsorbed on the inner surface of the catalysts, and with temperature increased, its intensity decreased, indicating desorption of NO_2 at higher temperature. As the relative intensity of bidentate nitrate and monodentate nitrate species was not significant, the time-dependent spectra were obtained at ~180 °C to further investigate the NO and O_2 adsorption/desorption behaviors on catalyst, as shown in Fig. 6(B).

When 250 ppm NO (balanced with N_2) was introduced, the peaks intensity increased with time. The existence of NO_2 related peak indicated that NO can react with surface oxygen to form NO_2. The peak at 1288 cm^{-1} can be assigned to monodentate nitrate and it shifted to 1341 cm^{-1}, which can be ascribed to *cis*-dimer nitroso. When O_2 was introduced to the flue gas, the nitrate peaks first increased and then decreased. However, the NO_2 peaks increased with time. This indicated nitrate may be an important intermediate to form NO_2, and it can be easily desorbed from the catalyst surface. Interestingly, the peaks related to *cis*-dimer nitroso disappeared after introducing O_2, suggesting it was rapidly oxidized by oxygen to form NO_2.

3.4 Proposed mechanism of NO catalytic oxidation on $Ni_2Mn_4Ce_4$

From the results of surface elements distribution, temperature programmed reduction analysis, we obtained that the existence of $Ni^{3+} + Mn^{3+} \rightarrow Ni^{2+} + Mn^{4+}$ and $Ce^{4+} + Ni^{2+} \rightarrow Ni^{3+} + Ce^{3+}$. Higher valence manganese was the main sites for NO catalytic oxidation. From the *in situ* DRIFTs, the main intermediates were bidentate nitrate and monodentate nitrate species. Therefore, a mechanism based on the above experimental results was proposed, as shown in Fig. 7. The surface –M–O–M–

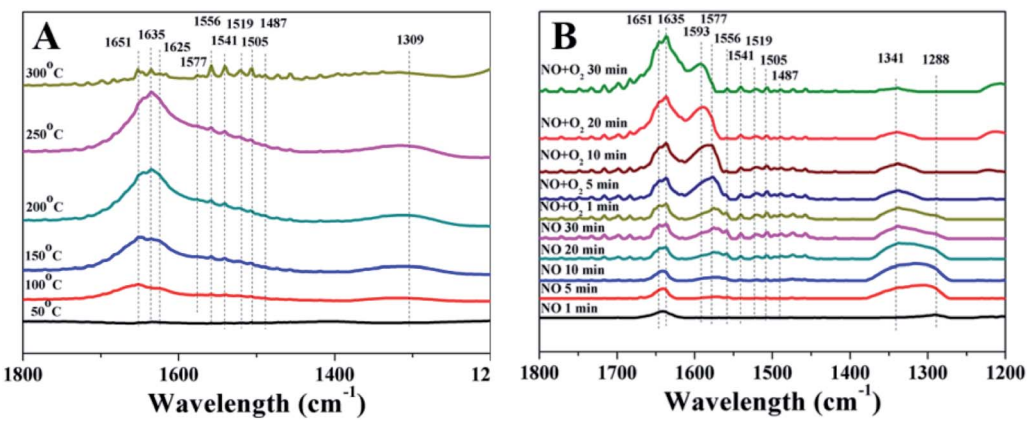

Fig. 6 *In situ* DRIFTs spectra of $Ni_2Mn_4Ce_4$ catalysts exposed to (A) NO + O_2/N_2 at different temperatures; (B) NO + N_2 and NO + O_2/N_2 at 200 °C.

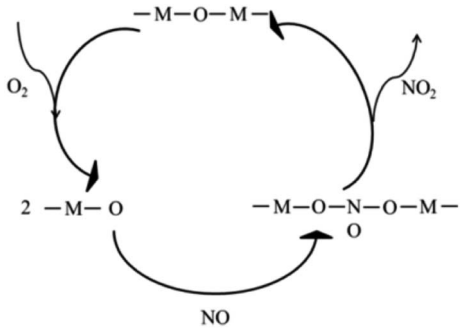

Fig. 7 A possible NO oxidation mechanism of as-prepared samples.

firstly reacted with oxygen to form –M–O, and then the later species was reacted with gaseous NO to form nitrates intermediates. At proper temperature, the nitrates intermediates were easily decomposed into gaseous NO_2, and the metal–oxygen species was returned to original states to form a complete catalytic circle.

3.5 SO_2 resistance of different catalysts

In practical conditions, SO_2 that co-existed with NO may influence the catalytic oxidation of NO. Studies of NO oxidation in the existence of SO_2 ($Ni_2Mn_4Ce_4$ and Mn_6Ce_4) were conducted, and the results were shown in Fig. 8. When SO_2 was introduced, the NO conversion rate was decreased for both two catalysts. When the temperature was above ~270 °C, the activity decrease was not significant; mainly because the reaction is thermodynamic limited at higher temperature. However, at the lower temperature range, the NO conversion rate dropped drastically. For example, the NO conversion rate for Mn_6Ce_4 and $Ni_2Mn_4Ce_4$ dropped by 25.29% and 13.15% at 180 °C, respectively. $Ni_2Mn_4Ce_4$ had a better SO_2 resistance compared with its counterpart without nickel, because nickel may decrease SO_2 adsorption, similar with our previous study.[14]

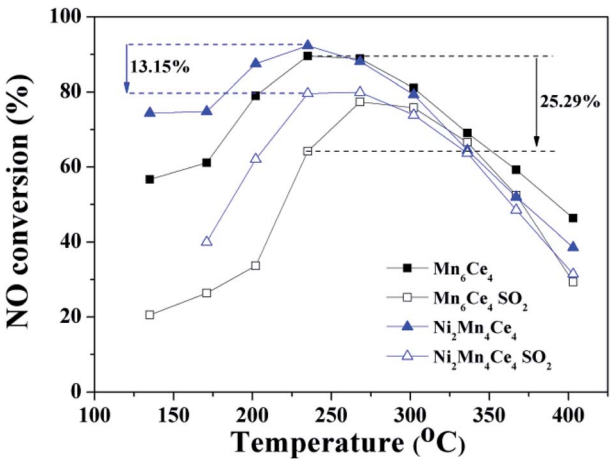

Fig. 8 NO oxidation performances of Mn_6Ce_4 and $Ni_2Mn_4Ce_4$ in presence of SO_2 (200 ppm).

4 Conclusions

In this paper, a series of mesoporous Ni–Mn–Ce ternary oxides were fabricated for NO catalytic oxidation, and the properties were characterized by various experiments. The $Ni_2Mn_4Ce_4$ catalyst showed a 95% NO conversion rate at 210 °C. The introduction of nickel into Mn–Ce composites can regulate the ratio of surface oxygen and manganese species, therefore improving the NO catalytic oxidation. Compared with other catalysts, $Ni_2Mn_4Ce_4$ exhibited a higher specific surface area, lower reduction temperature, more surface Mn^{4+} species, which led to its higher NO oxidation activity. XPS results can provide proofs for $Ni^{2+} + Ce^{4+} \rightarrow Ce^{3+} + Ni^{3+}$, and $Ni^{3+} + Mn^{3+} \rightarrow Ni^{2+} + Mn^{4+}$. From the results of *in situ* DRIFTs, a possible mechanism was proposed, in which nitrates species were main intermediates. The SO_2 resistance experiments showed that nickel addition can increase SO_2 durability of catalysts, mainly because nickel may decrease SO_2 competitive adsorption on catalysts.

Conflicts of interest

There are no conflicts to declare.

Acknowledgements

The research was financially supported by the National Key Research and Development Plan (2016YFC0204100, 2016YFC0204103), Control Strategy and Technology Integrated Demonstration of Industrial Source Pollution in Guanzhong area of China (ZDRW-ZS-2017-6-2). The authors also acknowledge the analytical and testing center of Institute of Process Engineering, Chinese Academy of Sciences, for their extensive help in testing of samples.

References

1 (*a*) G. Busca, L. Lietti, G. Ramis and F. Berti, *Appl. Catal., B*, 1998, **18**, 1; (*b*) P. G. Smirniotis, P. M. Sreekanth, D. A. Peña and R. G. Jenkins, *Ind. Eng. Chem. Res.*, 2006, **45**, 6436.
2 L. J. Alemany, L. Lietti, N. Ferlazzo, P. Forzatti, G. Busca, E. Giamello and F. Bregani, *J. Catal.*, 1995, **155**, 117.
3 H. Hu, S. X. Cai, H. R. Li, L. Huang, L. Y. Shi and D. S. Zhang, *ACS Catal.*, 2015, **5**, 6069.
4 S. Adjimi, J. M. García-Vargas, J. A. Díaz, L. Retailleau, S. Gil, M. Pera-Titus, Y. Guo and A. Giroir-Fendler, *Appl. Catal., B*, 2017, **219**, 459.
5 C. Ciardelli, I. Nova, E. Tronconi, D. Chatterjee and B. Bandl-Konrad, *Chem. Commun.*, 2004, 2718.
6 J. Li, W. H. Goh, X. Yang and R. T. Yang, *Appl. Catal., B*, 2009, **90**, 360.
7 (*a*) Z. Wu, N. Tang, L. Xiao, Y. Liu and H. Wang, *J. Colloid Interface Sci.*, 2010, **352**, 143; (*b*) F. Meng, S. Zhang, X. Li, Y. Zeng and Q. Zhong, *Mol. Catal.*, 2019, **473**, 110393.
8 W. Cai, Q. Zhong, J. Ding and Y. Bu, *Chem. Eng. J.*, 2015, **270**, 1.
9 Z. Hong, Z. Wang and X. Li, *Catal. Sci. Technol.*, 2017, **7**, 3440.

10 (*a*) M. Machida, M. Uto, D. Kurogi and T. Kijima, *J. Mater. Chem.*, 2001, **11**, 900; (*b*) P. Sudarsanam, B. Hillary, M. H. Amin, S. B. A. Hamid and S. K. Bhargava, *Appl. Catal., B*, 2016, **185**, 213.
11 (*a*) N. Tang, Y. Liu, H. Wang and Z. Wu, *J. Phys. Chem. C*, 2011, **115**, 8214; (*b*) K. Li, X. Tang, H. Yi, P. Ning, D. Kang and C. Wang, *Chem. Eng. J.*, 2012, **192**, 99.
12 (*a*) H. Chen, Y. Wang and Y.-K. Lyu, *Mol. Catal.*, 2018, **454**, 21; (*b*) S. J. Ma, X. W. Wang, T. Chen and Z. H. Yuan, *Chem. Eng. J.*, 2018, **354**, 191.
13 T. Zhang, H. Li, Z. Yang, F. Cao, L. Li, H. Chen, H. Liu, K. Xiong, J. Wu, Z. Hong and W. Wang, *Appl. Catal., B*, 2019, **247**, 133.
14 W. M. Li, H. D. Liu and Y. F. Chen, *RSC Adv.*, 2019, **9**, 11912.
15 S. Lai, Y. She, W. Zhan, Y. Guo, Y. Guo, L. Wang and G. Lu, *J. Mol. Catal. A: Chem.*, 2016, **424**, 232.
16 Z. Liu, Y. Yi, S. Zhang, T. Zhu, J. Zhu and J. Wang, *Catal. Today*, 2013, **216**, 76.
17 F. Kleitz, S. Hei Choi and R. Ryoo, *Chem. Commun.*, 2003, 2136.
18 Z. Wang, F. Lin, S. Jiang, K. Qiu, M. Kuang, R. Whiddon and K. Cen, *Fuel*, 2016, **166**, 352.
19 F. Gao, X. Tang, H. Yi, C. Chu, N. Li, J. Li and S. Zhao, *Chem. Eng. J.*, 2017, **322**, 525.
20 B. Zhao, R. Ran, X. Wu and D. Weng, *Appl. Catal., A*, 2016, **514**, 24.
21 X. Tang, J. Chen, X. Huang, Y. Xu and W. Shen, *Appl. Catal., B*, 2008, **81**, 115.
22 C. Lamonier, A. Ponchel, A. D'Huysser and L. Jalowiecki-Duhamel, *Catal. Today*, 1999, **50**, 247.
23 T. Zhu and M. Flytzani-Stephanopoulos, *Appl. Catal., A*, 2001, **208**, 403.
24 G. Long, M. Chen, Y. Li, J. Ding, R. Sun, Y. Zhou, X. Huang, G. Han and W. Zhao, *Chem. Eng. J.*, 2019, **360**, 964.
25 X. Hu, L. Huang, J. Zhang, H. Li, K. Zha, L. Shi and D. Zhang, *J. Mater. Chem. A*, 2018, **6**, 2952.
26 Y. Wan, W. Zhao, Y. Tang, L. Li, H. Wang, Y. Cui, J. Gu, Y. Li and J. Shi, *Appl. Catal., B*, 2014, **148–149**, 114.
27 X. Zhou, X. Lai, T. Lin, J. Feng, Z. Hou and Y. Chen, *New J. Chem.*, 2018, **42**, 16875.
28 H. Li, W. K. Ho, J.-j. Cao, D. Park, S. C. Lee and Y. Huang, *Environ. Sci. Technol.*, 2019, **53**, 10906.
29 Y. Xie, J. Wu, G. Jing, H. Zhang, S. Zeng, X. Tian, X. Zou, J. Wen, H. Su, C.-J. Zhong and P. Cui, *Appl. Catal., B*, 2018, **239**, 665.
30 W. Tang, M. Yao, Y. Deng, X. Li, N. Han, X. Wu and Y. Chen, *Chem. Eng. J.*, 2016, **306**, 709.
31 W. Xu, G. Zhang, H. Chen, G. Zhang, Y. Han, Y. Chang and P. Gong, *Chin. J. Catal.*, 2018, **39**, 118.
32 S. R. Kirumakki, B. G. Shpeizer, G. V. Sagar, K. V. R. Chary and A. Clearfield, *J. Catal.*, 2006, **242**, 319.
33 J. Liu, X. Li, R. Li, Q. Zhao, J. Ke, H. Xiao, L. Wang, S. Liu, M. Tadé and S. Wang, *Appl. Catal., A*, 2018, **549**, 289.
34 (*a*) C. Tang, J. Li, X. Yao, J. Sun, Y. Cao, L. Zhang, F. Gao, Y. Deng and L. Dong, *Appl. Catal., A*, 2015, **494**, 77; (*b*) J. Zhang, Y. Cao, C.-A. Wang and R. Ran, *ACS Appl. Mater. Interfaces*, 2016, **8**, 8670.
35 (*a*) G. Qi and R. T. Yang, *J. Phys. Chem. B*, 2004, **108**, 15738; (*b*) H. Wang, H. Chen, Y. Wang and Y.-K. Lyu, *Chem. Eng. J.*, 2019, **361**, 1161; (*c*) C. C. Dinerman and G. E. Ewing, *J. Chem. Phys.*, 1970, **53**, 626.
36 G. Zhou, B. Zhong, W. Wang, X. Guan, B. Huang, D. Ye and H. Wu, *Catal. Today*, 2011, **175**, 157.